PERGAMON

International Journal of Heat and Mass Transfer 42 (1999) 673–683

International Journal of HEAT and MASS TRANSFER

Effect of an unsteady external flow on mass transfer to cavities

Ahmed K. Shehata[a], J. Deliang Yang[b], Alan C. West[b], Vijay Modi[a,*]

[a] *Department of Mechanical Engineering, Columbia University, New York, NY 10027, U.S.A.*
[b] *Department of Chemical Engineering, Columbia University, New York, NY 10027, U.S.A.*

Received 26 March 1998; in final form 15 June 1998

Abstract

Mass transfer to the bottom wall of a rectangular cavity in the presence of an external periodic flow is investigated. Flow unsteadiness is generated by placing a circular cylinder at mid height within a channel. The cavity is located downstream of the cylinder at the lower wall of the channel. Both experimental measurements and numerical simulations are carried out to establish the ability of a time-accurate finite element solver to capture the transient flow and mass transfer. The mass-transfer rate at the bottom wall of the cavity is measured using reduction of ferricyanide ions on a platinum line electrode. Cavity aspect ratios (height/width) of 0.5, 1.0 and 1.81 and Reynolds numbers based on channel heights between 100 and 800 are investigated.

Nomenclature

c concentration [mol cm^{-3}]
c_∞ bulk concentration [mol cm^{-3}]
D diffusion coefficient [cm^2 s^{-1}]
d diameter of cylinder [cm]
F Faraday's constant, 96 487 C mol^{-1}
h channel height [cm]
h_c cavity height [cm]
i current density [mA cm^{-2}]
L electrode half length [cm]
N molar flux [mol cm^{-2} s^{-1}]
Q volume flow rate [cm^3 s^{-1}]
Q_{in} flow into cavity [mm^2 s^{-1}]
Nu mass transfer Nusselt number
Nu_{no} mass transfer Nusselt number in the absence of a blocking cylinder
Re Reynolds number based on the channel height
Sc Schmidt number
u velocity [cm s^{-1}]
u_{avg} average velocity in the sensor region of the cell [cm s^{-1}]
u_m experimental mean velocity in the x direction [cm s^{-1}]
w channel width [cm]
w_c cavity width [cm]
v kinematic viscosity [cm^2 s^{-1}]
x, y Cartesian coordinates [cm].

Greek symbol
τ sampling time [s].

1. Introduction

Convective mass or heat transport from small cavities has many engineering applications. For example, metallization processes for electronic packaging or interconnects involves electrochemical deposition into very small cavities which have been created by technologies such as photolithography. As miniaturization proceeds the aspect ratio of the cavities tends to increase. As aspect ratios increase, the mixing inside a cavity becomes weak due to the formation of recirculating eddies. Hence improving the communication of the fluid inside the cavity with external flow can increase the rate of mass transport. One means of increasing communication is to introduce flow instabilities that interrupt the formation of the recirculating eddies.

There have been many investigations of mass or heat transport inside a cavity where the flow is steady and

* Corresponding author. Tel.: 001 212 854 2956; Fax: 001 212 854 3304; E-mail: modi@columbia.edu

0017–9310/98 $19.00
PII: S0017–9310(98)00218–X

laminar [1–11]. It has long been recognized that flow instabilities can increase the mass or heat transfer rate. Ghaddar et al. [12, 13] investigated the flow pattern inside a cavity when the channel flow is destabilized by upstream cavities. It was found that the resulting unsteady flow enhanced the heat-transfer rate to the bottom surfaces of downstream cavities. Pulsed flow has also been investigated extensively. It was found that the mass transfer rate was enhanced only if flow reversal occurred [14].

Mass transfer to a channel wall downstream of a suspended cylinder in a channel has been investigated previously [15]. It was shown that unsteady flow was generated in the presence of a blocking cylinder suspended in a flow channel and that the local mass-transfer rate depends upon the distance downstream of the cylinder. A periodically reappearing local recirculation region near the wall was observed several diameters downstream of a blocking cylinder (see Fig. 1), in the Reynolds number range of 200–800. This recirculation region was found to be associated with the location of the large amplitude of oscillation of mass-transfer rate. While this location varied with Reynolds number, cylinder diameter and possibly with time, the measurements indicated this position to be about 4.1 cylinder diameters downstream of the blocking cylinder in the mid-range of the Reynolds numbers of interest for a d/h of 0.50. It was hoped that placing a cavity at this position would lead to a relatively large change in mass-transfer due to flow unsteadiness. The mass-transfer to the bottom wall of the cavity is examined for cavity aspect ratios of $h_c/w_c = 0.0$, 0.5, 1.0 and 1.81. Cylinders diameter of $d/h = 0.25$ and 0.5 are examined. For comparison, mass transfer to the cavity in the absence of a blocking cylinder is also considered. An electrochemical method, reduction of ferricyanide ion on a line platinum electrode, is used to measure the mass-transfer rate.

2. Experimental

A flow channel designed to provide a fully developed flow at the blocking cylinder was used. A schematic diagram of the flow channel is shown in Fig. 2. The channel was constructed out of transparent Plexiglas, with a removable plate to access the test section. The channel has cross-sectional dimensions $h \times w = 1.86 \times 9.53$ cm and is 132.1 cm long. The channel is the same as described in Yang et al. [15] where further details can be found.

The removable plate on which the cavities were fabricated was 9.53×9.15 cm plate., A slit of 0.21×2.0 cm was made at plate mid-width. A platinum foil of 0.19×1.99 cm is glued to the tip of a separate block indicated as WE in Fig. 2. The active width of the electrode $2L = 0.19$ cm is smaller than the cavity width $w_c = 0.21$ cm because a nonconductive varnish was coated at the sides of the platinum foil. The block is then inserted into the slit of the opening. The cavity aspect ratio is changed by using multiple gaskets. The entire measuring section is flush-mounted into the flow channel. The cavity and the working electrode are located 68.58

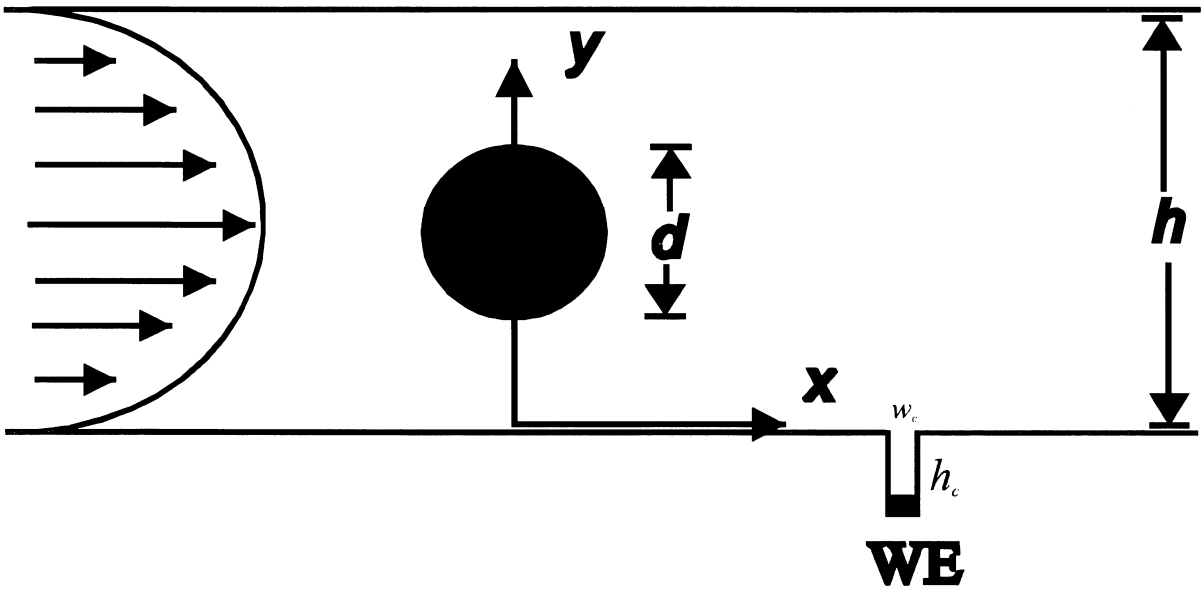

Fig. 1. Schematic of the cell. A working electrode (WE) of length $2L$ is placed at the bottom wall of the cavity, located a distance x downstream from a cylinder of diameter d. The cylinder is placed at the channel center. A fully developed parabolic flow is obtained upstream of the cylinder.

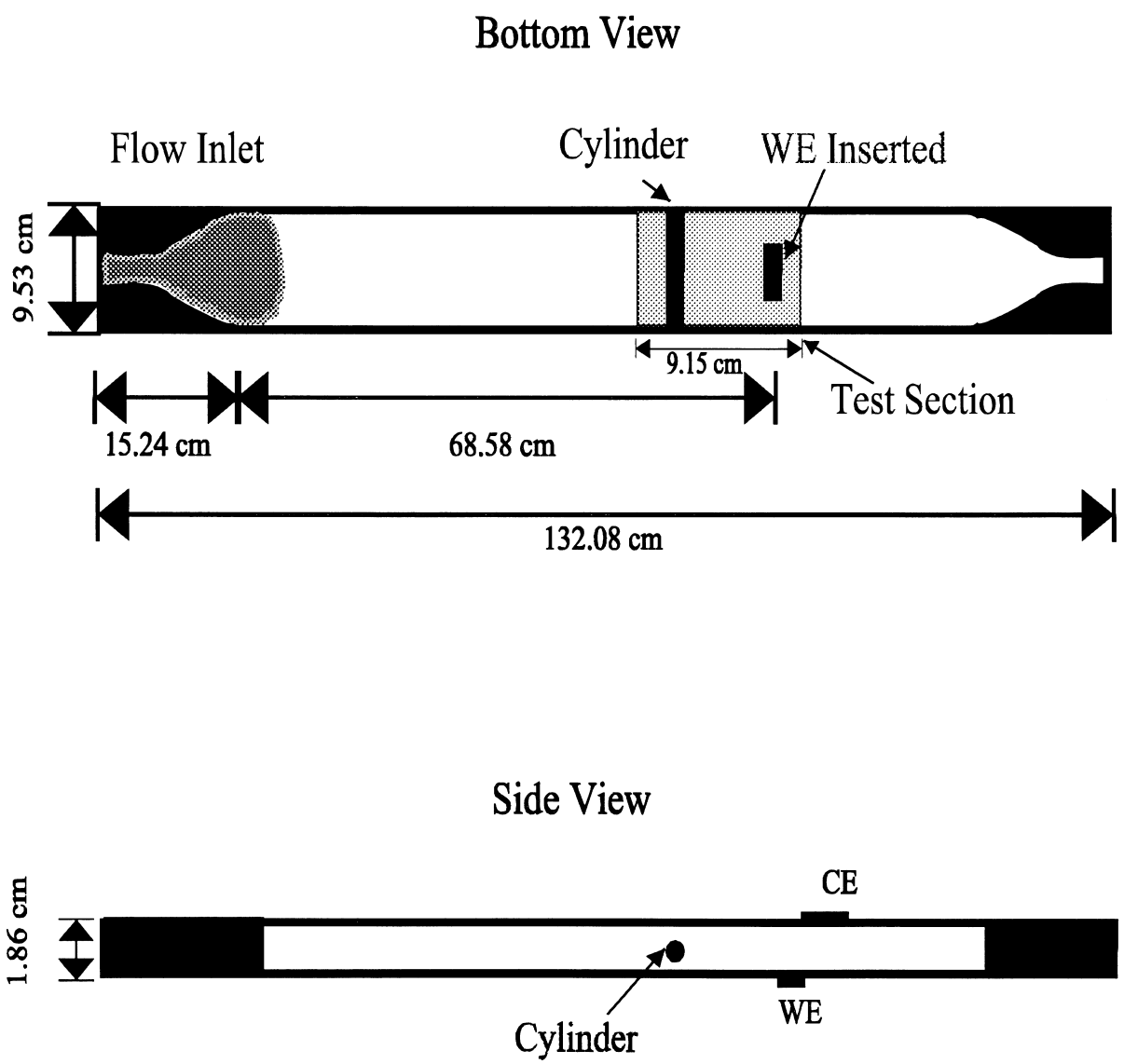

Fig. 2. Experimental setup. The contoured entrance and exit regions as well as the glass beads at the entrance region help minimize entrance and exit effects. Electrolyte is pumped into the channel from left to right. WE—working electrode, CE—counterelectrode.

cm downstream of the inlet region. The counterelectrode is placed on the upper channel wall slightly downstream of the working electrode.

A Plexiglas circular cylinder of uniform diameter ($d = 0.465$ cm or $d = 0.953$ cm) was placed at mid-height in channel as shown in Figs 1 and 2. The location of the cylinder could be adjusted as described in Yang et al. [15]. For the present study, it was placed at $x/d = 4.1$ upstream of the cavity. The uncertainty in cylinder position is ± 0.05 cm. The measuring section was screwed to the bottom plate and the counterelectrode was mounted flush at the top wall, slightly downstream of the cavity. Glass beads were mounted at the entrance to depress flow disturbances. A more detailed description of the design of the channel can be found in Yang et al. [15].

All experiments used 7 l of electrolyte composed of 0.003 M potassium ferricyanide, 0.003 M potassium ferrocyanide, and 0.1 M potassium chloride. The temperature was $23 \pm 2°C$. The diffusivity of the ferricyanide ion was determined to be $D = 0.8 \times 10^{-5}$ cm^2 s^{-1} corresponding to a Schmidt number, Sc, of 1250 [15]. The circulating electrolyte volume flow rate, Q, was varied from 10 to 86 cm^3 s^{-1} using a variable-speed gear pump for high flow rates and a small centrifugal pump for low

flow rates. These flow rates correspond to a mean channel velocity u_m ($=Q/(hw)$) of 0.47–4.2 cm s^{-1}. Due to the finite aspect ratio of the channel the average velocity near the sensor, u_{avg}, is higher than u_m and is given by $u_{avg} = 1.15\ u_m$ as shown in Natarajan and Lakshmanan [16]. The fluid flow can be characterized with a Reynolds number defined as

$$Re = \frac{u_{avg} h}{v} \tag{1}$$

where the kinematic viscosity $v = 10^{-2}$ cm^2 s^{-1} and h is the channel height.

To ensure that a quasisteady state was reached the flow rate was maintained constant for a period of time before data were taken. This time exceeded 1 h for the cavity aspect ratio of 1.81. The rate of mass transfer to the electrode is reported in terms of a time and space averaged mass transfer Nusselt number:

$$Nu = \frac{NL}{Dc_\infty} = \frac{1}{2c_\infty \tau} \int_0^\tau \int_{-L}^{L} \left.\frac{\partial c}{\partial y}\right|_{\text{electrode}} \mathrm{d}x\, \mathrm{d}t \tag{2}$$

where τ is the sample time, N is the molar flux, L is the half length of the electrode, c_∞ is the bulk concentration, and D is the diffusion coefficient. The Nusselt number can be related through Fick's and Faraday's laws to the measured time-averaged current density i_{avg}

$$Nu = \frac{i_{avg} L}{FDc_\infty} \tag{3}$$

where F is the Faraday's constant and i_{avg} is assumed to be positive. Even though a dynamic measurement of current at a sampling frequency of 1000 Hz was carried out, the measured currents for all cavity aspect ratios were always found to be steady unlike the flush-sensor results of Yang et al. [15].

3. Numerical simulations

Numerical simulations were performed using a finite element code for the fluid flow and a finite volume code for the concentration solution. Both the codes permit time-accurate solutions in a two-dimensional domain.

The fluid flow solver is briefly described here. The primitive-variable form of the continuity and momentum equations are solved using a finite element procedure detailed in Wasfy et al. [17]:

$$\frac{\partial u_x}{\partial t} + u_x \frac{\partial u_x}{\partial x} + u_y \frac{\partial u_x}{\partial y} = -\frac{1}{\rho}\frac{\partial P}{\partial x} + v\left(\frac{\partial^2 u_x}{\partial x^2} + \frac{\partial^2 u_x}{\partial y^2}\right) \tag{4}$$

$$\frac{\partial u_y}{\partial t} + u_x \frac{\partial u_y}{\partial x} + u_y \frac{\partial u_y}{\partial y} = -\frac{1}{\rho}\frac{\partial P}{\partial y} + v\left(\frac{\partial^2 u_y}{\partial x^2} + \frac{\partial^2 u_y}{\partial y^2}\right) \tag{5}$$

$$\frac{\partial u_x}{\partial x} + \frac{\partial u_y}{\partial y} = 0. \tag{6}$$

The standard Galerkin approximation, which reduces to a central difference type of scheme is used. A semi-explicit procedure with equilibrium iterations at each time step is used. Even though the flow is incompressible, the compressible flow equations in their incompressible limit were solved for computational reasons [17]. This approach artificially reduces the propagation speed of a disturbance (which is theoretically infinite for incompressible flows) allowing larger time steps [17]. The computational domain is divided into quadrilateral elements and conventional bilinear interpolation is used for both the velocity and pressure. The odd–even decoupling of the pressure field is eliminated by the use of a pressure averaging technique. The code has been validated against several steady as well as unsteady benchmark fluid flow problems [17]. The flow field was solved on the domain A–B–C–D–E–F–G–H–I–J–A shown in Fig. 3.

A fully developed parallel flow with a parabolic velocity profile was specified at the channel inlet:

$$u_x = 1.5 u_{avg}\left[1 - \left(\frac{2y}{h} - 1\right)^2\right], \quad u_y = 0. \tag{7}$$

The pressure at the channel exit was assumed uniform across the channel height. No-slip conditions for velocity were specified at both the upper and lower walls as well as the cylinder boundary: $u_x = u_y = 0$.

The computational domain was truncated at a distance 7.5 cylinder diameters downstream of the entrance since the measurements are made at a position 4.1 diameters downstream of the cylinder. This truncation of the domain was found to be appropriate from previous calculations [15]. Grids were generated using a commercial software package, GridPro [18], primarily to ensure that deviation of grid elements from orthogonality was minimized.

At the high Schmidt numbers ($Sc = 1250$) of interest in the present study, the gradients in concentration can be an order of magnitude (approximately proportional to $Sc^{1/3}$) greater than the gradients in flow. Consequently the concentration solver requires a grid that is an order of magnitude finer than the flow solver. This would have required a prohibitively large number of grid points for the concentration solver. It is however unnecessary to solve for the concentration in the regions upstream and downstream of the cavity where no significant concentration gradients occur. Consequently a smaller domain B–C–D–E–H–I–B shown in Fig. 3 was utilized to solve for the concentration. In this smaller domain it was possible to use a much finer grid than that for the fluid flow.

An upwind finite volume scheme was used to solve the convection–diffusion equation:

$$\frac{\partial c}{\partial t} + u_x \frac{\partial c}{\partial x} + u_y \frac{\partial c}{\partial y} = D\left(\frac{\partial^2 c}{\partial x^2} + \frac{\partial^2 c}{\partial y^2}\right). \tag{8}$$

Boundary conditions at I–B as well as H–I, were set to the

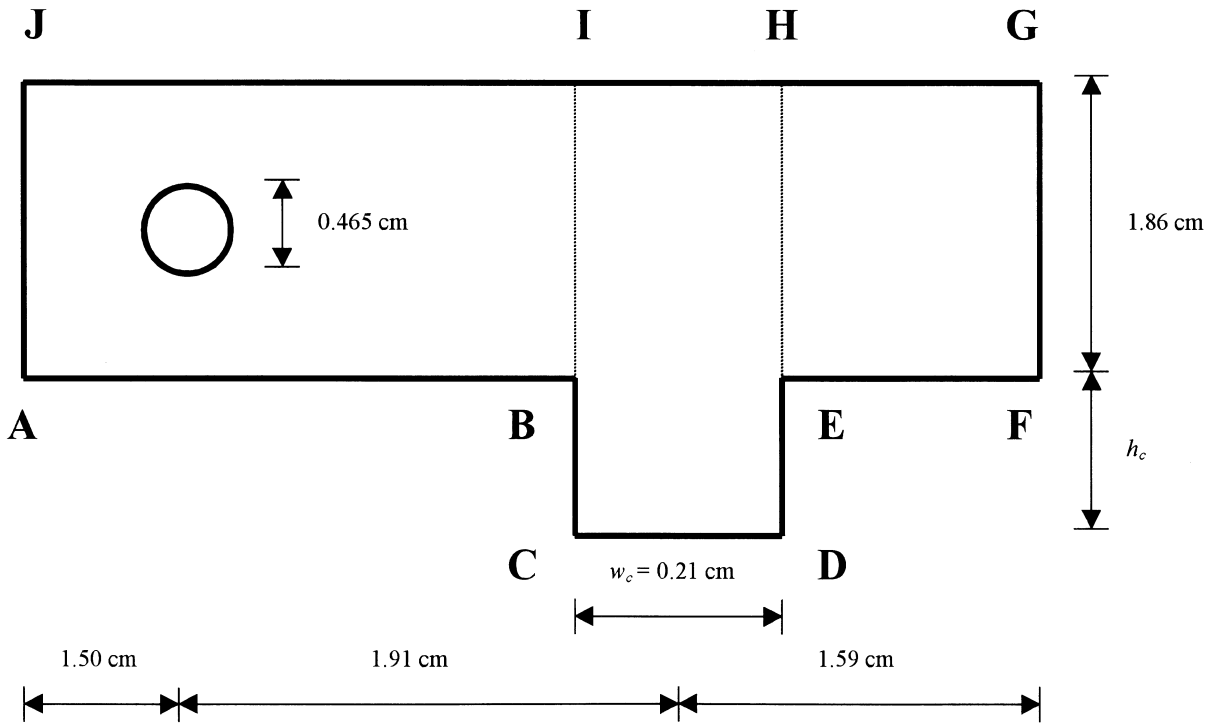

Fig. 3. A schematic diagram of the computational domains used for simulation of the flow field and concentration field. The larger domain A–B–C–D–E–F–G–H–I–J–A is for the flow solution. The smaller domain B–C–D–E–H–I–B is for the concentration solution. This diagram is specific for the case of $d/h = 0.25$ and h_c varies with the cavity aspect ratio. The schematic diagram is not drawn to scale.

bulk concentration value, while at E–H the concentration gradient in the channel flow direction is set to zero. The concentration gradient normal to the cavity side walls, B–C and D–E, is also set to zero. At the electrode surface, C–D, the concentration is set to zero.

The velocity field obtained from the fluid flow solver did not perfectly satisfy continuity in the region inside the cavity. Even though these errors were small, they could lead to erroneous concentration solutions. Hence the velocity field was modified by applying a continuity satisfying correction to the u_y velocity component, assuming that the u_x component is accurate. The possible exception to this case is the time dependent flow for a cavity aspect ratio of 1.81. The higher errors in continuity for this case are discussed later.

Since the flow solver uses a general quadrilateral type of element and the concentration solver uses a cartesian grid, an interpolation of the velocity data was needed for use in the concentration solver. This was carried out using bilinear interpolation functions, that were also used to approximate the velocities in the flow solver.

A grid independence test for the fluid flow solution was carried out with three different meshes of 3400, 5800 and 8900 elements. Given the possibly unsteady nature of the flow, it is desirable to verify grid independence at a location where the effect of unsteadiness is strongly felt. Hence the y-velocity component at the cavity mouth was selected for comparison. The time variation of $u_y(x)$ along the cavity mouth was plotted at several instances of time during a single period. Two snapshots, representing the envelope of this time variation during the entire cycle are then plotted for each of the three grids in Fig. 4. These envelopes demonstrate that the results from all the three grids are essentially the same. All the calculations reported here had at least the grid density corresponding to that of the 5800 element grid. The smallest grid size was 1/20 of the cavity width. The grid Re (Reynolds number based on, Δx, typical size of an element) in the primary flow was around 12 whereas inside the cavity the values varied from 1–10^{-4} (for $h_c/w_c = 1.81$).

Once the fluid flow was solved to an acceptable accuracy a grid independence test was also carried out for the concentration solver using three different meshes 30×40, 60×80 and 100×200. The results for the two finest grids were within 3% of each other and hence all the calculations were carried out with the 100×200 grid. The grid Peclet numbers ($u_x \Delta x/D$) was about 15 000 in the primary flow whereas inside the cavity the values varied from 8 to 10^{-3} (for $h_c/w_c = 1.81$).

The time-steps and the time needed to reach a quasi-

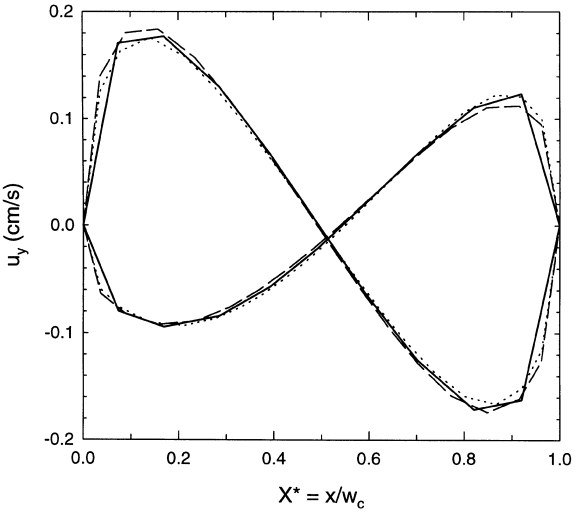

Fig. 4. Variation of the u_y velocity component along the cavity mouth with grid refinement during a single period. Two snapshots representing the envelope of time variation for each grid are shown for cavity aspect ratio $h_c/w_c = 0.50$, $Re = 364$ and $d/h = 0.50$. Number of elements = 3423 (solid line), 5816 (dashed line) and 8804 (dotted line).

steady state vary with the Reynolds number and the geometry. For simulations at $Re = 600$ and $d/h = 0.25$ quasi-steady periodic fluid flow was achieved at a physical time $t = 10$ s. Since the period of oscillation of the flow is about 0.5 s this corresponds to approximately 20 periods. The number of time steps in each period was about 1600, corresponding to a *CFL* number [17] of about 4 for interior elements.

4. Results and discussion

In contrast to flush mounted results [15], the current measurements are steady for all cavity sizes. The cavity mass transfer rates obtained from numerical simulations are also found to be steady even when the fluid flows are unsteady.

Numerical simulations were carried out for $d/h = 0$ (no cylinder), 0.25 and 0.5 with cavity aspect ratios $h_c/w_c = 0$ (no cavity), 0.5, 1.0 and 1.81. The Reynolds numbers for the simulations were selected to extend from 100–800. The lower limit was chosen to correspond to steady flow even in the presence of a cylinder. Since the simulations are two-dimensional, the results are applicable up to Reynolds numbers at which three-dimensional effects first appear. Experimental studies [15, 19–21] suggest that three-dimensional effects first appear at Reynolds numbers of 190–260 based on cylinder diameter. Hence the Reynolds numbers were limited to 800 for $d/h = 0.25$ and 466 for $d/h = 0.50$. Results are reported in terms of a Nusselt number, *Nu* as obtained from equation (2) to characterize the space and time-averaged mass-transfer rate. It turned out however that the computed Nusselt numbers even in the unsteady flow regime were time invariant.

Simulations were first carried out in the absence of a cylinder for $200 < Re < 800$ for $h_c/w_c = 0.5$, 1.0 and 1.81. The variation of *Nu* with *Re* is shown in Fig. 5 along with the experimental values. The results indicate that the mass transfer rate increases with increasing flow through the channel. This increase appears to be greater for the smallest aspect ratio. The numerical simulations were able to capture this trend.

Simulations were next carried out in the presence of a cylinder with $d/h = 0.25$ for $200 < Re < 800$. Simulated results for $Re = 200$ corresponding to Reynolds number based on cylinder diameter of 50 were found to be steady while unsteady periodic flow was observed at larger Reynolds numbers. The variation of the computed Nusselt numbers with *Re* is shown in Fig. 6 along with the experimental values. Results are shown for $h_c/w_c = 0$, 0.5, 1.0 and 1.81. The numerical simulations are able to capture the variation of *Nu* with *Re* except for the $h_c/w_c = 1.81$.

Finally simulations in the presence of a cylinder with $d/h = 0.5$ were carried out for $100 < Re < 466$ for $h_c/w_c = 0$, 0.5, 1.0 and 1.81. Simulated results for $Re = 100$, corresponding to a Reynolds number based on cylinder diameter of 50 were found to be steady while unsteady periodic flow was observed at larger Reynolds numbers. Figure 7 shows the variation of *Nu* number with *Re* for both numerical and experimental values. Again, numerical simulations are able to capture the variation of *Nu* with *Re* except for $h_c/w_c = 1.81$.

The above reported mass transfer measurements and numerical simulations reveal some interesting features

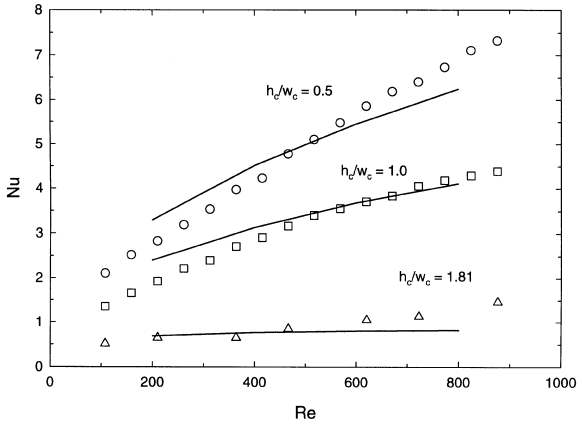

Fig. 5. Comparison of experimental (open symbols) and numerical (solid lines) variation of Nusselt number with *Re* in the absence of a blocking cylinder. Results shown for cavity aspect ratios $h_c/w_c = 0.5$, 1.0 and 1.81.

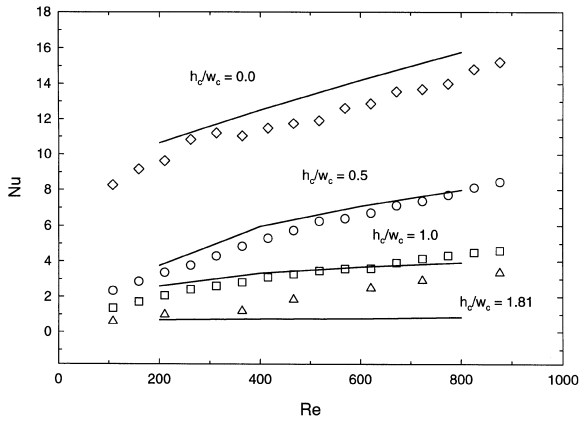

Fig. 6. Comparison of experimental (open symbols) and numerical (solid lines) variation of Nusselt number with *Re* in the presence of a blocking cylinder with $d/h = 0.25$. Results shown for cavity aspect ratios $h_c/w_c = 0$, 0.5, 1.0 and 1.81.

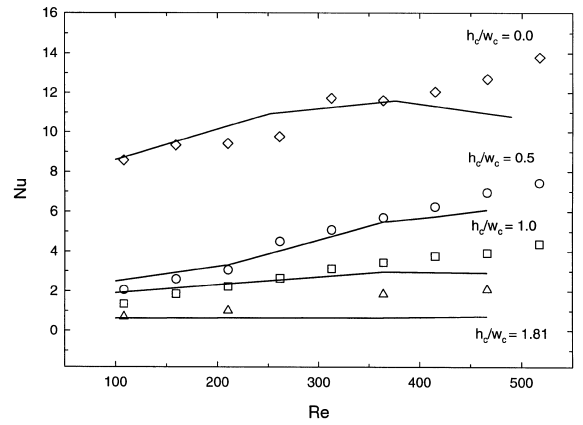

Fig. 7. comparison of experimental (open symbols) and numerical (solid lines) variation of Nusselt number with *Re* in the presence of a blocking cylinder with $d/h = 0.50$. Results shown for cavity aspect ratios $h_c/w_c = 0$, 0.5, 1.0 and 1.81.

of cavity mass transfer driven by an external unsteady laminar flow. These and the inability of the simulations to capture mass transport at $h_c/w_c = 1.81$ are discussed below.

The experiments reveal that for the same flow rate the presence of a blocking cylinder leads to increased mass transfer rate at the bottom of a cavity wall. It is easier to see this increase when the experimental data of Figs 5–7 are expressed as Nu/Nu_{no} where Nu_{no} is the Nusselt number in the absence of a cylinder. The measured variation of Nu/Nu_{no} with *Re* for each of the three cavity aspect ratios is plotted in Fig. 8(a)–(c). Data for both $d/h = 0.25$ and 0.50 are shown. Enhanced mass transfer, indicated by Nu/Nu_{no} greater than unity, is observed for all cases even though no systematic trend can be cited. One obser-

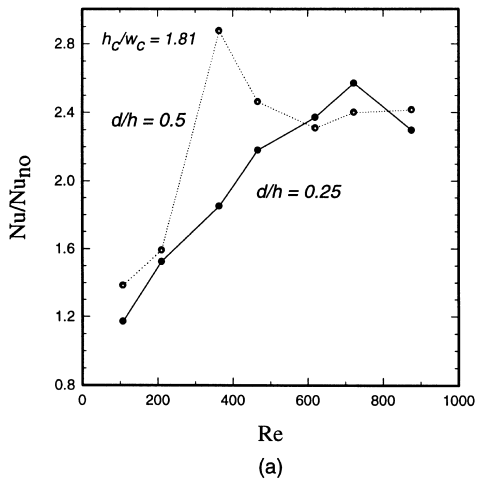

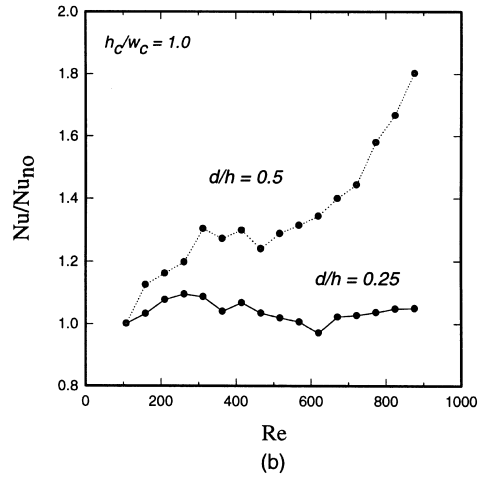

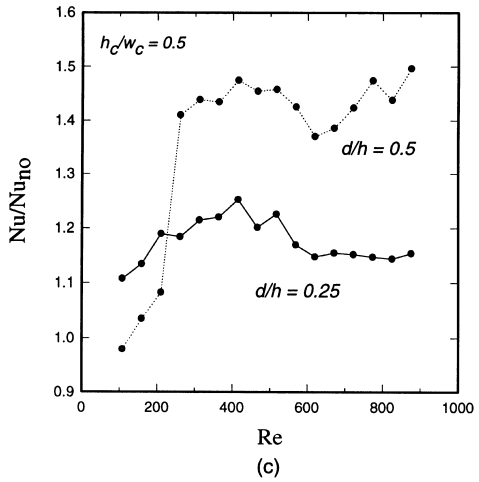

Fig. 8. Variation of experimental Nu/Nu_{no} with *Re* for $d/h = 0.25$ and 0.50. Here *Nu* and Nu_{no} are Nusselt number with and without a blocking cylinder. Cavity aspect ratios h_c/w_c (a) 1.81, (b) 1.0 and (c) 0.50.

vation that is clear however is that at Reynolds numbers where the flow external to the cavity is steady, enhancement is either absent or small.

The mechanism responsible for the enhanced mass transfer rate is the vertical exchange of momentum driven by the Karman vortex street. A measure of this exchange is the average rate at which fluid enters (or leaves) the cavity mouth during one period. This quantity Q_{in} (in $mm^2\ s^{-1}$) is obtained from the computed fluid flow solutions for $d/h = 0.25$ for each of the three cavities. These results are shown in Fig. 9 along with the Q_{in} values for channel flow in the absence of a blocking cylinder. Observe that the Q_{in} values for the unsteady flow ($Re > 200$ for the $d/h = 0.25$ case shown) are an order of magnitude larger than the Q_{in} values for the steady flow cases. Here the steady flow cases include the $Re = 200$ case for $d/h = 0.25$ when the flow is steady even in the presence of a blocking cylinder. These results confirm the role of the exchange of fluid (between the cavity flow and the flow external to the cavity) in enhancing mass transfer.

For $h_c/w_c = 1.81$ the numerical simulations were unable to predict the increase in mass transport associated with the unsteady flows for both $d/h = 0.25$ and 0.50. Some understanding of this inability can be obtained from the flow pattern within the cavities for the steady flow case of $Re = 200$ for $d/h = 0.25$. Steady state streamlines for the three cavities are shown in Fig. 10. Note that since the flow external to the cavity is essentially the same for the three cases, a single plot is shown in Fig. 10(a). The streamline plots reveal the existence of a single primary eddy for $h_c/w_c = 0.50$ and 1.0 whereas for 1.81

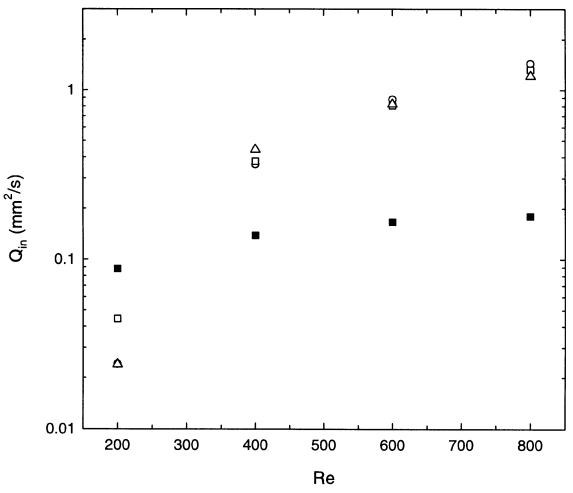

Fig. 9. Variation of the volume flow rate into the cavity, Q_{in} ($mm^2\ s^{-1}$), with Re for $d/h = 0$ (solid symbols) and $d/h = 0.25$ (open symbols) with $h_c/w_c = 0.50$ (square), 1.0 (circle) and 1.81 (triangle). The Q_{in} values for $d/h = 0$ are identical for $h_c/w_c = 0.50$, 1.0 and 1.81.

there is an additional smaller secondary eddy present as well. In Fig. 11, the absolute value of the u_x velocity component is plotted along mid-width of the cavity from the bottom wall of the cavity to a position one cavity width above the lower channel wall. Fig. 11 also shows that the velocity profiles at the cavity mouth ($y^* = y/w_c = 0$) are nearly the same regardless of the cavity size. The average speeds in the primary eddy are two to three orders of magnitude lower than those in the external flow. For the $h_c/w_c = 1.81$ case, the secondary eddy, driven by the primary eddy, has speeds that are four to five orders of magnitude lower than the external flow speeds.

The disparity in the wide range of flow speeds between the inside and outside of the cavity has some implications to the accuracy of the flow solution. As the flow speeds reduce, the otherwise negligibly small time-derivative of pressure term introduced in the continuity equation by the artificial compressibility method [17] may begin to compete with the order of the spatial derivatives $\partial u_x/\partial x$ or $\partial u_y/\partial y$. In the external channel flow this error is less than 0.1%, whereas when a single primary eddy is present we estimate this error to be between 0.1 and 1%. However when a secondary eddy is present, as is the case for the aspect ratio 1.81 cavity, this error can be as large as 10%. This may preclude our ability to accurately model flows where the low speed secondary eddy is indeed time-dependent. Note that these errors are only related to time-dependent solutions, since for steady flows the artificial time-derivative of pressure vanishes.

The discrepancy between numerical and experimental results could also be due to the possibility of high sensitivity of the flow to geometric parameters, in particular the distance of the cavity from the blocking cylinder. There may be other reasons as well, though less likely, such as the presence of natural convection in the vicinity of the electrode, or presence of three-dimensional flow structures that could contribute to the discrepancy.

The streamline plots of Fig. 10 and the velocity profiles of Fig. 11 suggest that the flow structure at the cavity mouth is remarkably similar regardless of the cavity aspect ratio at least for steady flows. Does the flow at the cavity mouth continue to be independent of the cavity aspect ratio even when the external flow becomes unsteady? If this is indeed the case it would have beneficial implications for the modeling of high aspect ratio cavities. To determine this, the time variation of $u_y(x)$ along the cavity mouth was examined in a fashion similar to Fig. 4 for each cavity at $Re = 364$ for $d/h = 0.50$. The results are shown in Fig. 12. They demonstrate that the flow entering the cavity is essentially independent of the cavity aspect ratio. This conclusion is also supported by the nearly identical Q_{in} values for the unsteady cases shown in Fig. 9 for $d/h = 0.25$. This suggests that the weak flow fields of high aspect ratio cavities may be possibly simulated by carrying out a separate computation of the

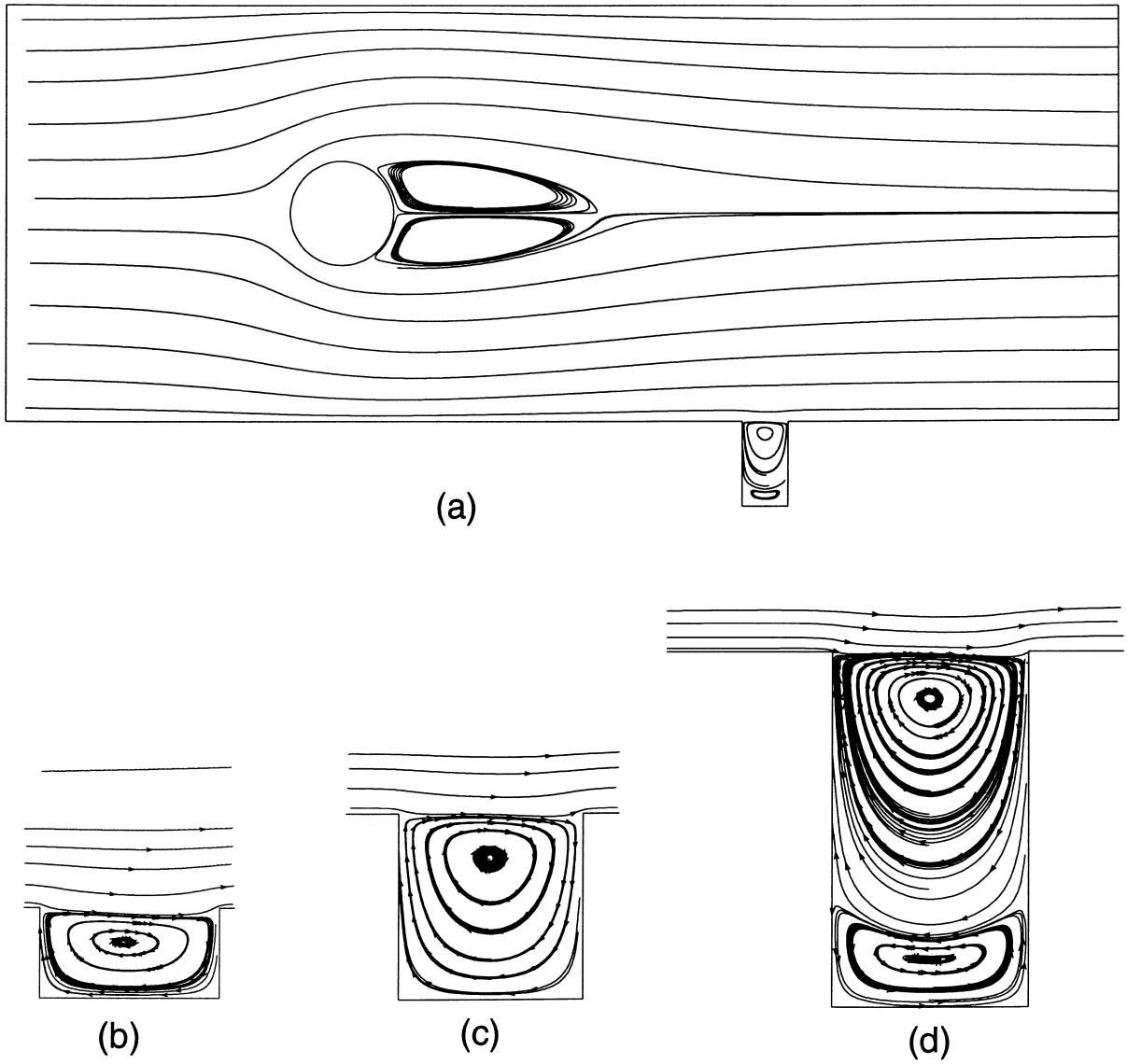

Fig. 10. Computed steady flow streamlines at $Re = 200$ for $d/h = 0.25$. The primary channel flow shown in (a) is identical for three cavity aspect ratios. Flows shown in (b), (c) and (d) for $h_c/w_c = 0.5$, 1.0 and 1.81, respectively.

cavity flow alone with an imposed flow field at the cavity mouth.

6. Conclusions

An experimental and numerical study of mass transfer to the bottom wall of a cavity in the presence of an external unsteady flow was carried out. A periodic unsteadiness, produced by a Karman vortex street downstream of a cylinder in an otherwise steady channel flow, was shown to increase the mass transfer rate to the cavity bottom wall. The enhancement was found to depend upon the cavity aspect ratio as well as the diameter of the blocking cylinder for given channel flow rate.

A numerical model was developed and validated to capture the unsteady laminar two-dimensional fluid flow and the associated mass transfer. In the range of *Re* numbers where one expects the flow to be two-dimensional, the model was successful in predicting the mass transfer to the cavity. The effect of flow unsteadiness produced by a blocking cylinder led to an order of magnitude increase in the volume flow rate into and out of the cavity. The flow structure at the cavity mouth and

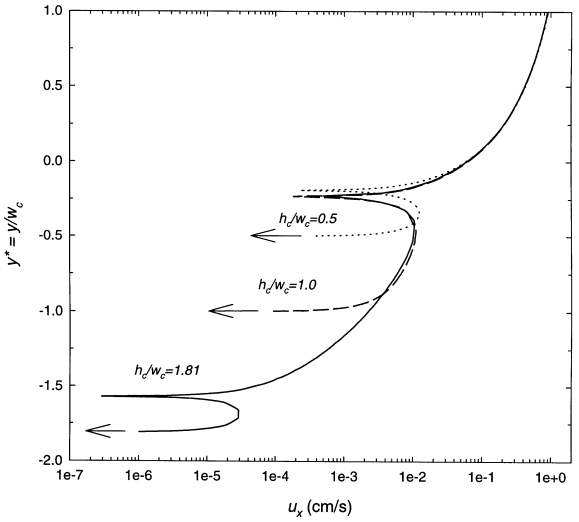

Fig. 11. Variation of the absolute value of $u_x(y)$ at cavity mid-width starting from the cavity bottom wall and ending at a position one cavity width above the lower channel wall. Numerical results are shown for three cavity aspect ratios $h_c/w_c = 1.81$, 1.0 and 0.50 for simulations at $Re = 200$ and $d/h = 0.25$ (steady flow). Arrows indicate that those values go to zero.

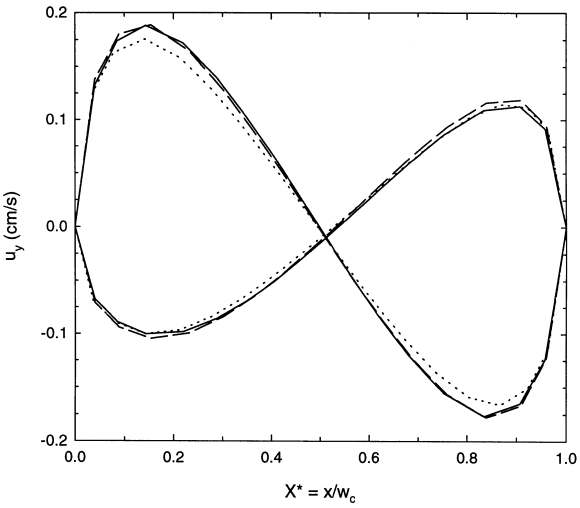

Fig. 12. Two snapshots representing the envelope of time variation of the $u_y(x^*)$ at the cavity mouth during a single cycle for each cavity aspect ratio $h_c/w_c = 1.81$ (solid line), 1.0 (dashed line) and 0.50 (dotted line). Results are for simulation at $Re = 364$ for $d/h = 0.50$.

the volume flow rate into the cavity were found to be nearly independent of the cavity aspect ratio. The model however was unable to capture the increase in mass transfer measured experimentally for a cavity aspect ratio of 1.81. This inability may be associated with the presence of a secondary eddy that is four to five orders of magnitude weaker than the primary channel flow.

Acknowledgements

This work was supported by the National Science Foundation under Grant nos CTS-93-15991 and CTS-97-06824. The authors would like to thank Dr Tamer M. Wasfy for the development and continued assistance in the use of the fluid flow solver.

References

[1] R. Beck, Effect of hydrodynamics on pitting, Corrosion 33 (1977) 9.
[2] R. Beck and S.G. Chan, Experimental observations and analysis of hydrodynamic effects on small pits, Corrosion 37 (1981) 665.
[3] C. Alkire, D.B. Reiser, R.L. Sani, Effect of fluid flow on removal of dissolution products from small cavities, J. Electrochem. Soc. 131 (1984) 2795.
[4] Harb, R.C. Alkire, Transport and reaction during pitting corrosion of Ni in 0.5 M NaCl: II. Flowing fluid, J. Electrochem. Soc. 138 (1991) 3568.
[5] C. Alkire, H. Deligianni, Jeh-Beck Ju, Effect of fluid flow on convective transport in small cavities, J. Electrochem. Soc. 137 (1990) 818–824.
[6] M. Occhialini, J.J.L. Higdon, Convective mass transport from rectangular cavities in viscous flow, J. Electrochem. Soc. 139 (1992) 2845–2855.
[7] C. Alkire, H. Deligianni, The role of mass transfer on anisotropic electrochemical pattern etching, J. Electrochem. Soc. 135 (1988) 1093.
[8] B. Shin, D.J. Economou, Forced and natural convection effects on the shape evolution of cavities during wet chemical etching, J. Electrochem. Soc. 138 (1991) 527.
[9] O'Hern, J.R. Torczynski, T.K. Blanchat, T.Y. Chu, A.L. Tassin, Shear-driven flow in a square cavity: a comparative study using PIV, LDV, computational simulations, Laser Anemometry 1994 Advances and Applications ASME, Fluids Engineering Division, 1994, DED-vol. 191, p. 135.
[10] H. Chen, Effect of the aspect ratio on the transient mass/heat transfer in an open cavity, J. of the Chinese Inst. of Engineers 19 (1996) 273.
[11] N. Chang, H.W. Ryu, D.H. Park, Y.S. Park, Effect of external laminar channel flow on mass transfer in a cavity, Int. J. Heat Mass Transfer 30 (1987) 2137–2149.
[12] K. Ghaddar, K.Z. Korczal, B.B. Mikic, A.T. Patera, Numerical investigation of incompressible flow in grooved channels. Part 1. Stability and self-sustained oscillations, J. Fluid Mech. 163 (1986) 99–127.
[13] K. Ghaddar, M. Magen, B.B. Mikic, A.T. Patera, Numerical investigation of incompressible flow in grooved channels. Part 2. Resonance and oscillatory heat-transfer enhancement, J. Fluid Mech. 168 (1986) 541–567.
[14] L. Guinon, V. Perez-Herranz, J. Garcia-Anton, G. Lacoste, Enhancement of mass transfer at a spherical electrode in pulsating flow, J. Appl. Electrochem. 25 (1995) 267.

[15] Yang, A. Shehata, V. Modi, A.C. West, Mass transfer to a channel wall downstream of a cylinder, Int. J. Heat Mass Transfer 40 (1997) 4263–4271.
[16] Natarajan and Lakshmanan, Laminar flow in rectangular ducts: prediction of velocity profiles and friction factor, Indian J. of Tech. 10 (1972) 435–438.
[17] T. Wasfy, A.C. West, V. Modi, Parallel finite element computation of unsteady incompressible flows, Int. J. Numer. Meth. Fluids 26 (1998) 17–37.
[18] GridPro/az3000, User's guide and reference manual, Program Development Corporation, White Plains, New York, 1996.
[19] Williamson, C.H.K., Vortex dynamics in the cylinder wake, Annu. Rev. Fluid Mech. 28 (1996) 477–539.
[20] H.K. Williamson and A. Roshko, Measurement of base pressure in the wake of a cylinder at low Reynolds numbers, Z. Flugwiss. Weltraumforsch. 14 (1990) 38–46.
[21] D. Henderson and D. Barkley, Secondary instability in the wake of a circular cylinder, Phys. Fluids 8 (1996) 1683–1685.